SAND2022-5548C

ASTFE American Society of Thermal and Fluids Engineers

Proceedings of the 2nd Thermal and Fluid Engineering Conference, TFEC2017

4th International Workshop on Heat Transfer, IWHT2017

April 2-5, 2017, Las Vegas, NV, USA

TFEC-IWHT2017-18058

THERMOCHEMICAL MODEL OF INTUMESCING FIRE PROTECTION COATING

Larsen, M. E*, Reinholz, E.L., Coker, E. N., Jameson, K. J., Hoffmeister, K. N. G., Adee, S. M.

Sandia National Laboratories
P.O. Box 5800, Albuquerque, NM 87185

ABSTRACT

Protective coatings are in wide use to limit damage to equipment and facilities at risk of fire hazards. The effectiveness of a commercially available intumescing fire-protection coating was quantitatively assessed in laboratory tests simulating a half-hour hydrocarbon fuel fire. The coating was applied to a stainless steel metal substrate and exposed to thermal radiation from a parallel plate driven to 1024°C to simulate the fire boundary condition. Chemical reactions occurring from approximately 300 to 900°C outgas and expand the material to approximately twenty times its initial volume and one-third of its initial mass. The rates of chemical decomposition were characterized through thermogravimetric analyses (TGA) and used to inform Arrhenius kinetics models.

A finite element model formulation incorporates the chemistry to describe the transient conversion of the layer to the expanded state. The unreacted layer is opaque to radiation and of relatively high thermal conductivity. In the expanded/reacted condition the layer provides significant insulating benefit to slow the thermal insult to the substrate. At elevated temperatures the reacted layer's heat transfer is dominated by thermal radiation which is adequately represented by the diffusion method. Comparisons are included between the experimental data and the model.

KEY WORDS: Computational methods, Fire protection, Thermochemical

1. INTRODUCTION

The present investigation is motivated by a requirement to develop a thermally-resistant wall design with an intumescent passive fire protection (PFP) coating. Such coatings are frequently used to maintain structural integrity of steel [1-5], aluminium [6], laminates [7], and glass fiber-reinforced epoxy (GRE) composite [8] substrates to protect buildings, ships [6], liquefied petroleum gas tanks [9], and other industrial or petrochemical environments both on- and offshore in the event of hydrocarbon pool fires or jet fire impingement [5]. Tests such as UL-1709 and NORSOK M-501 provide thermal response, physical endurance, and weathering resistance performance data [5]. Yet, even with these stringent testing standards, evaluation of

*Corresponding Author:melarse@sandia.gov

specific designs and applications would benefit largely from improved modeling of intumescent materials (IMs). Many IM models exist; most are one-dimensional mathematical models that include kinetics, gas evolution and entrapment, and/or IM expansion [1-3, 10,11]. To the best of our knowledge, only Asaro et al. [6] and Landucci et al. [9] have developed finite element (FE) IM models. Asaro [6] applied simplified kinetics for a single-stage reaction, where other authors have shown that IMs experience oxidative degradation in three reactions [3,12]. Landucci et al. [9] used constant thickness and properties with no inclusion of thermochemical changes in their FE model. We strive to better characterize the thermochemical behavior of an IM using a finite element model. Like Di Blasi et al. [4] and Branca et al. [7], we apply Arrhenius kinetics for a three-stage oxidative degradation process. The predicted reaction extent is then used to indicate the extent of transition of thermal transport properties from the virgin material to the fully reacted material.

Our design requires limits on the temperature excursion of the cooler side of a wall exposed to fire. The candidate design includes an IM layer that will decompose and expand when exposed to an abnormal operating environment of fire, creating a stable char layer. The concept is illustrated in Fig. 1. The char layer provides insulation when the fire persists beyond the IM decomposition. If the fire conditions continue well past the decomposition, the thermal resistance of a stable char may be more important than thermal response delay attributed to the decomposition reactions.

This investigation addresses the need for a better model to predict the thermal performance of the intumescing layer. Consider a uniform fire threat for the interval of system depicted in Fig. 1. Where there is substructure attached to the heated wall, conduction from the substrate to the substructure will generally suppress the temperature response resulting in spatially distributed decomposition progress even for a uniform boundary condition. A distribution of rates of decomposition progress will also result for any fire too small to fully engulf the system. Consequently, a model addressing the thermal response of a system must correctly predict rates of chemical decomposition and transport through the decomposition products for varied heating rates and maximum temperatures.

The next section describes thermal experiments performed on very small samples of the IM to extract kinetic parameters for chemical reaction rate predictions. Following that, experiments are described in which two-foot (0.6096m) by two-foot square wall sections protected by the IM were subject to a fire-like boundary condition which result in the full decomposition of the material. Next the FE model formulation is described which utilizes both the kinetic parameters and the observed heating rates from the larger scale experiments. Finally, the model is assessed against the available data and conclusions are presented.

2. EXPERIMENTAL METHODS AND RESULTS

2.1 Thermal Analyses

Method. Thermogravimetric analysis (TGA), differential thermal analysis (DTA), and mass spectrometry (MS) provided insight to the thermal decomposition of the intumescent material. A Netzsch STA 409 CD thermogravimetric/differential thermal analyzer (Netzsch, Selb, Germany) generated TGA/DTA data under a 100 ml min^{-1} flow of either argon (UHP grade, Matheson, Basking Ridge, NJ) or air (ultra-zero grade, Matheson) between 25 and 1100°C. A Hiden HPR-20 mass spectrometer (Hiden, Warrington, England) sampled the gas exiting the TGA/DTA furnace via a 2m heated capillary inlet. Specimens of intumescing material were cut from a sheet using a razor blade, and had dimensions of approx. 10 mm x 10 mm x 0.5 mm (mass ca. 160 mg). Each test specimen was placed in the bottom of a 5 ml alumina cup in the TGA/DTA instrument. Once sample mass and gas flow had reached steady state at 25°C, the TGA furnace was heated at a rate of 20, 30, 40, or 50°C·min^{-1} to 1100 °C (1200°C in the case of 50°C·min^{-1} ramp).

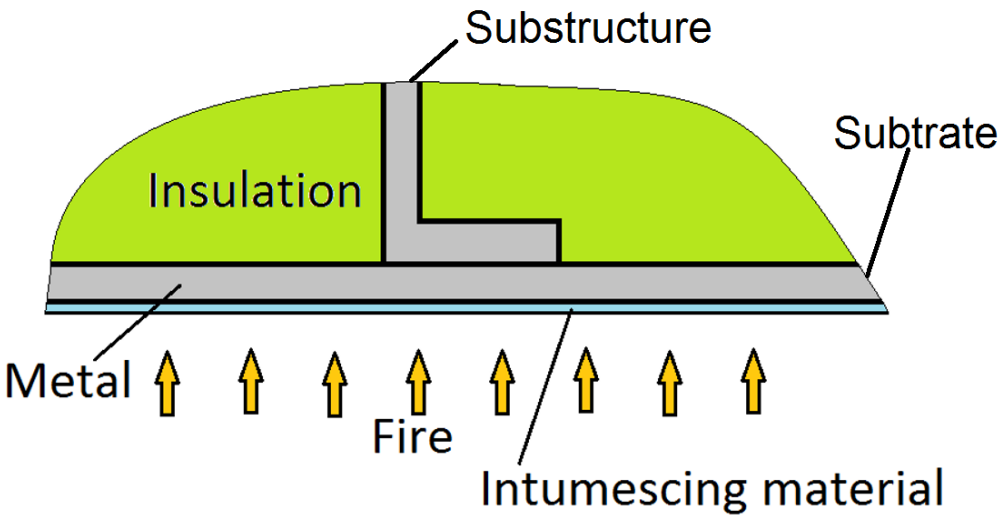

Fig. 1 Schematic representation of fire-threatened metal wall assembly protected by intumescent coat.

Baseline correction runs were conducted by running each temperature/gas profile with an empty specimen cup; the baseline TGA data was then subtracted from the specimen TGA data to remove artifacts due to buoyancy changes. An S-type thermocouple in contact with the bottom of the alumina specimen cup monitored the temperature of the specimen, which was used in data analysis (as opposed to the furnace temperature).

Results. Results are shown in Figs. 2 and 3, and the solid lines indicated in Fig. 8 show additional TGA data using multiple heating rates. The IM decomposition in argon and air differ significantly. Prior investigators [1, 2] showed that the concentration of oxygen in the reaction volume affected the thermal IM model. The differences the reaction profiles for argon vs. air shown in Figs. 2 and 3 support this theory.

The TGA/DTA results in Fig. 2 demonstrate that in argon, the mass loss occurs in a single step (300-450°C) indicative of single-step degradation. In air, oxidative degradation appears to occur in three steps (300-450°C, 450-620°C, and 700-900°C). Previous investigations have identified the three steps as melting, intumescence, and char formation [2,6]; in some cases, a fourth step (char degradation) was also mentioned [1]. The DTA data suggest broadly exothermic reactions for both argon and air runs.

The single decomposition reaction in argon evolves CO_2 and H_2O as the major off-gassing components (Fig. 3). In air, CO_2 and H_2O were the major off-gas components for the first two reactions, and CO_2 was the major off-gas component for the third reaction. Hydrocarbons were minor off-gas components for the first reaction in both air and argon runs (Fig. 3).

Kinetic parameters were extracted from the TGA data using the Ozawa/Flynn/Wall (OFW), Flynn and Wall [14-16], method followed by a MATLAB optimization similar to that of Charait, et al. [17]. Each of the three stages shown in the oxidative degradation TGA data (Fig. 2) was approximated as a separate reaction, with the extent of reaction, α, increasing from zero to one for each stage.

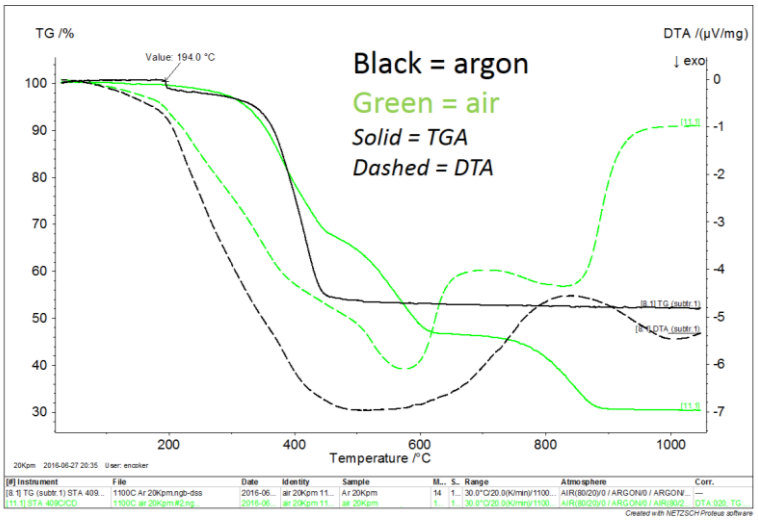

Fig. 2 TGA and DTA measurements performed on a sample of the IM, shown at 20°C·min^{-1}.

The optimization method solved the general first-order rate equation:

$$\frac{d\alpha}{dT} = \frac{A}{\beta}(1-\alpha)\exp[-E/RT] \tag{1}$$

where T is absolute temperature, A is the pre-exponential factor, β is the heating rate, E is the activation energy, and R is the gas constant. The optimization's search parameters included the pre-exponential factor and activation energy. The initial search parameters were derived using the OFW method and were optimized to minimize the error between $\alpha(T)_{experimental}$ and $\alpha(T)_{model}$ for a given β. The resulting values are shown in Table 1 of Section 4.2.

In addition to extraction of kinetic parameters and heats of reaction, the detailed measurements presented in Fig. 2 and Fig. 3 contributed to a broad understanding of the decomposition of the IM. For example, three reactions are apparent and gas is produced by each. Solid material remains throughout, with ~30% mass remaining at 1000°C. A more fundamental study of the IM chemistry was not conducted due to the apparent complexity of the material. An empirical model of the chemistry guided by the TGA/DTA data, OFW optimization model, and DSC analysis will be presented in Section 4.2.

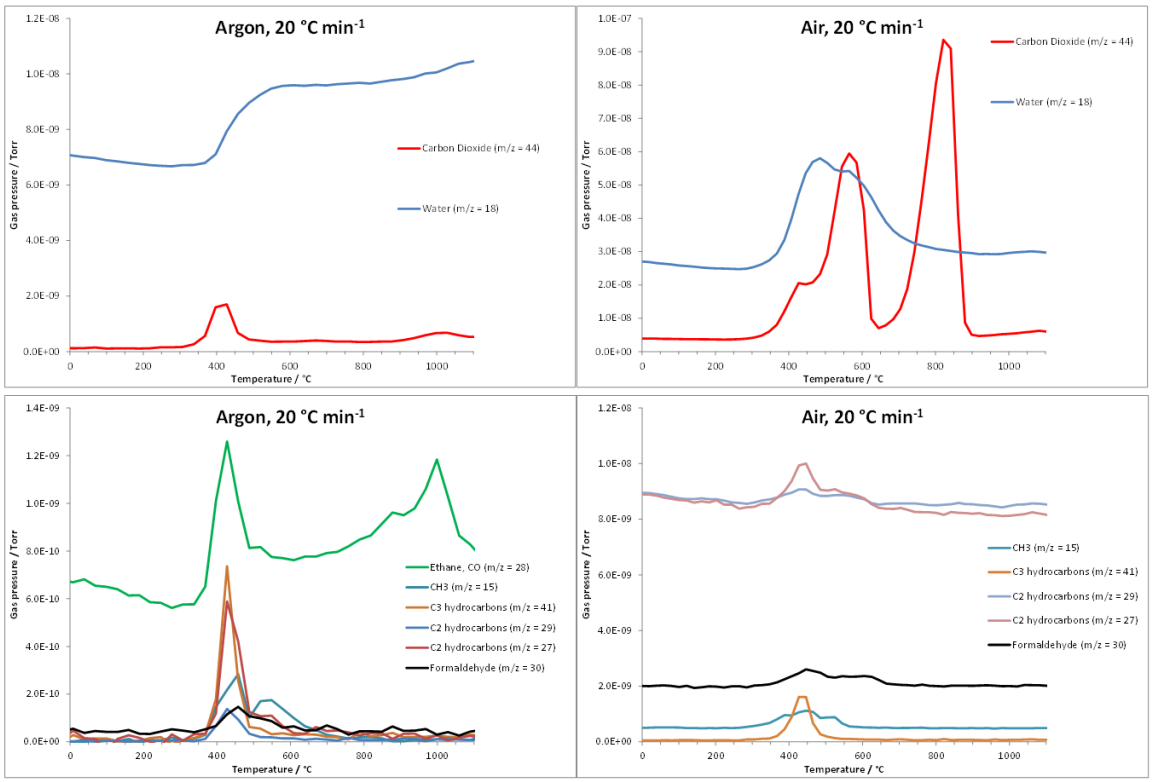

Fig. 3 Mass spectroscopy analysis for TGA products in argon and air environments. TGA was performed with a 20K/min heating rate.

3.1 Large Scale Tests.

Test Panel. The test panel was constructed of two flat two-foot (0.6096m) by two-foot sheets of 0.120 inch (3.048mm) 304L stainless steel, connected by a c-channel stud of the same metal and thickness. Each sheet was fully welded to the stud with a 0.125" (3.2mm) fillet weld on both sides of the stud. The wall stud was oriented vertically during the testing. The stainless steel had a finish of 2B from the steel supplier.

The 1.3mm thick intumescent material was installed on the outer side of the test panel using the adhesive backing on the material. The stainless steel substrate was cleaned with an alcohol based cleaner to remove any manufacturing oil and dirt prior to the peel-and-stick IM application.

Test apparatus. The two-foot (0.6096m) by two-foot square wall panel was mounted in a vertical plane. The outer side was exposed to thermal radiation from an Inconel shroud nominally heated to 1024°C (1875°F). The shroud was painted with PyroMark in an attempt to produce a blackbody radiator. Fig. 4 shows a sketch of the test stand features and a photograph of a test in operation. The 40" (1.016m) square shroud (purple in the left picture of Fig. 4) was irradiated on the backside with a total of 93 high-power (6kW) lamps in three vertical panels. Thermal modeling was used to develop a lamp position strategy with the goal of achieving a uniform shroud temperature. The 93 lamps were distributed over approximately 150 positions available with greater density in the corners and lesser density in the middle panel. Three liquid-cooled panels approximately one-foot (30.5mm) wide supported the 10" (25.4mm) lamps and provided an electrical bus and cooling air to the lamps. The voltage to the electrical bus of each panel was controlled independently to drive thermocouples

across from the panel midpoints to the prescribed temperature history of 1024°C in three minutes to maintain that temperature for 30 minutes after which the system was powered off.

As illustrated in Fig. 4, the planes containing the lamps, shroud, and test panel were parallel, with the lamps and test panel on each side of the shroud and one foot (30.5mm) from it. The test apparatus is shown in operation on the right view of Fig. 4. The sidewalls between the lamps and the shroud and those between the shroud and the test panel were insulated with ceramic fiber blanket insulation and rigid ceramic board insulation to create a nearly adiabatic wall. The use of blanketing rather than rigid board on the high temperature side of the shroud has proven to be effective because the roughly 1000°C temperature creates appreciable strain/growth in confined surfaces.

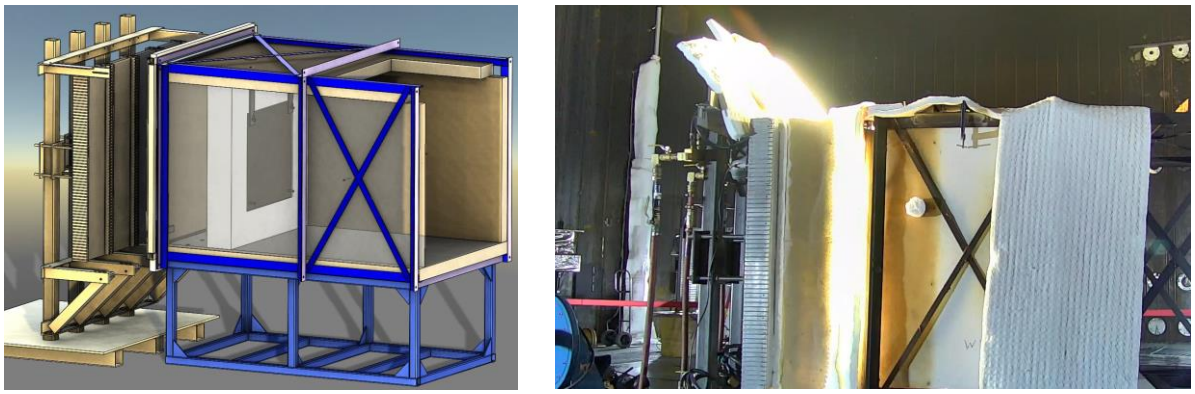

Fig. 4 Thermal test apparatus for wall panels.

Fig. 5 shows the temperature histories of shroud for a typical test. The control thermocouples follow closely the nominal schedule. The shroud temperatures shown in Fig. 5 from 5 to 30 minutes are at an average temperature of 1007°C with a standard deviation of 20°C which corresponds to an emissive blackbody power of 152 kW/m^2.

Measured thermal responses. Limited measurements were available for the substrate temperature response behind the IM. Fig. 6 shows temperatures measured by five thermocouples for the wall panel test. The panel was 2-ft (0.6096 m) on each side with the thermocouples positioned as shown on the figure's inset and behind the 1.3 mm layer of IM. At all locations, there were a time delays before any appreciable thermal response. A structural beam in the wall was centered under TC18. After about four minutes the responses began to separate because of the conduction response through the beam and TC18 exhibits the expected temperature suppression relative to the other thermocouples. The experiment's symmetry would support the expectation that the responses at TC16 and TC20 and those at TC17 and TC19 be nearly the same. Lack of symmetry in these responses may arise from lack of symmetry in the heating imposed by the test rig or from inhomogeneity in the resulting char layer.

At the end of the experiment the char layer would be expected to exhibit about 30% of initial density as was observed repeatedly through TGA experiments with the IM exposed to air. The resulting char layer was very fragile and the adhesive thermally degraded, so before the lamp power was turned off some material may have sloughed away, making the layer geometry not entirely consistent. TC16 and TC20 responses in Fig. 6 are

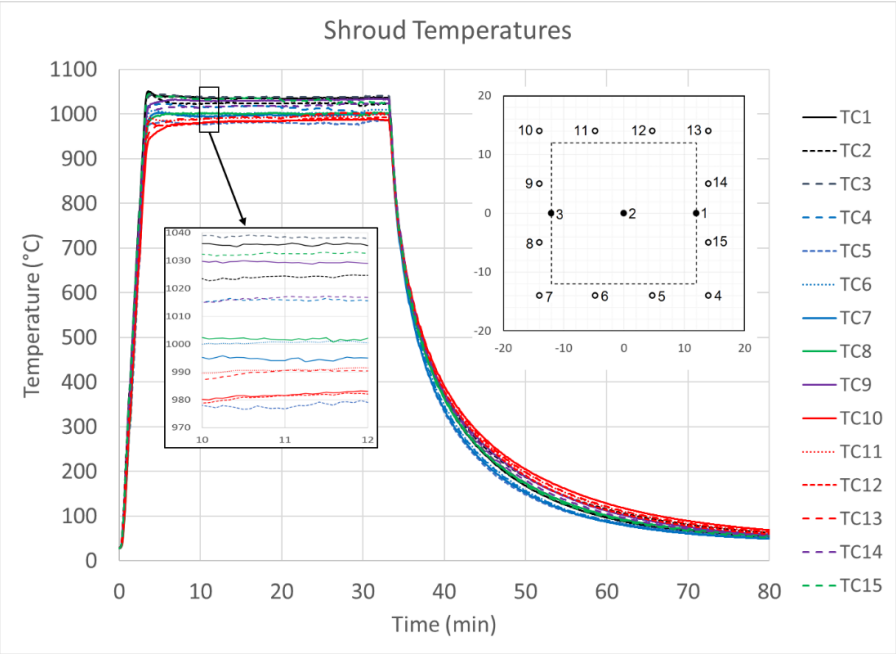

Fig. 5 Measured shroud temperature history and thermocouple locations (TC1, TC2, and TC3, the control locations, are indicated in the sketch by the filled circles).

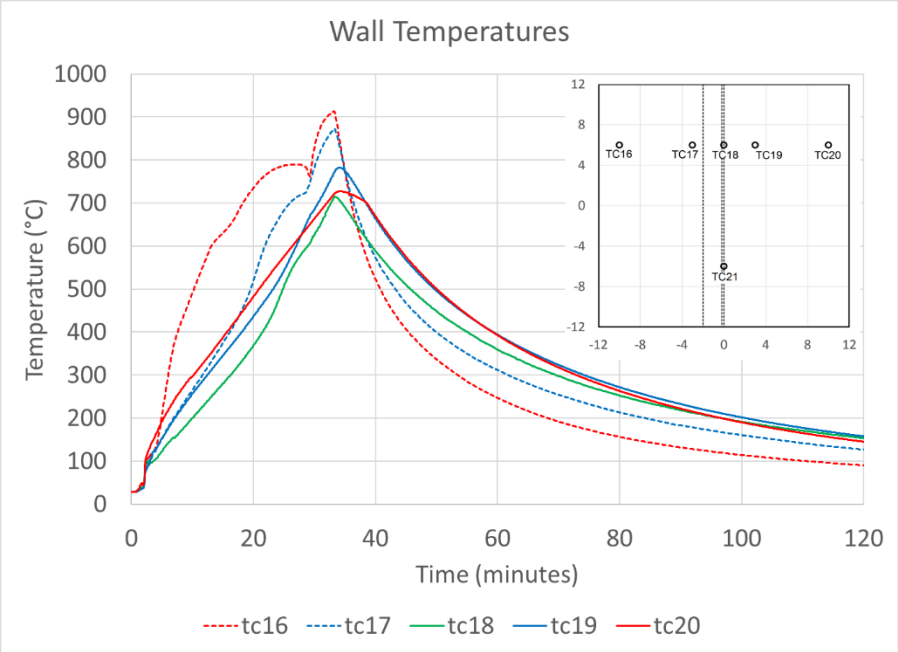

Fig. 6 Measured temperatures on substrate behind the IM.

those most distant from the beam in the center of the panel and lateral conduction in the substrate is expected to be small. In the following discussion, the responses of those locations will be compared to one-dimensional modeling. The disconcertingly large difference between the responses of TC16 and TC20 is greater than would be expected due to the unintended asymmetry of heating (see inset in Fig. 5) indicating a lack of uniform thermal protection. Shrinking of the cooling hot substrate after the lamp power was removed probably induced some separation of the IM. The discontinuity in the response of TC16 at about 30 minutes is likely the result of material loss from the char layer in the vicinity of the thermocouple.

In the post-test inspection the expanded IM resembles fibrous insulation but was weak and barely adhering to the plate. Fig. 7 shows a photo of a large piece of the expanded IM after the system was cooled and dismantled. The manufacturer's nominal specification for the product's expansion of 22:1 (28.6 mm or 1.125") was realized.

Fig. 7 Charred IM. Ruler shows inches.

4. THERMOCHEMICAL MODEL DESCRIPTION

4.1 General description of thermochemical model

The finite element code finds the transient temperature distribution $T(\boldsymbol{x}, t)$ that satisfies:

$$\rho C_p \frac{\partial T}{\partial t} = \nabla \cdot (k\nabla \mathrm{T}) + \dot{q}(\boldsymbol{x}) \tag{2}$$

over the modeled region. Eq. 2 indicates that the local rate of temperature change is created by conduction and other source terms in $\dot{q}(\boldsymbol{x})$. $\dot{q}(\boldsymbol{x})$ includes energy associated with chemical reactions, phase transition energies, and other transport mechanisms not addressed by the conduction term. In the intumescent region thermal conductivity can be expected to change dramatically with decomposition as the material changes from a relatively dense solid to an ashy char. The initial material is opaque to radiation but the expanded decomposition products may transfer energy through the thickness principally by thermal radiation.

4.2 Arrhenius chemical kinetics

A useful engineering model of the system of Fig. 1 may not require a detailed description of the many chemical species interacting during the decomposition of a complicated mixture. However, a general model must predict the onset and rates of decomposition of the intumescing material. For example, a region insufficiently heated to initiate decomposition needs to behave as the virgin material. Arrhenius kinetics informed by the foregoing TGA studies of the material are the foundation for modeling the decomposition in the finite element code used for this study.

Reactions were found which closely match measured mass loss curves for TGA experiments with samples exposed to air and heated at rates of 20, 30, 40, and 50°C/min. The shapes of the mass-loss curves for decomposition suggest three reactions and MS suggested that each generated gaseous species. The system was idealized as consisting of the following reactions:

$$M_{i-1} \rightarrow a_i M_i + (1 - a_i)G \quad \text{for} \quad i = 1, 2, 3 \tag{3}$$

M_0 is the unreacted IM and M_1, M_2 and M_3 are mass fractions of unspecified, condensed-phase products of decomposition. Each condensed material is the only condensed product of its "parent." G is any gaseous product which leaves the reaction with the purge gas. The rates of these reactions are modeled as:

$$r_i = B_i \exp(-E_i/[RT]) \tag{4}$$

where B_i are pre-exponential factors, E_i are activation energies, and a_i are stoichiometry coefficients for each of the reactions.

$$\frac{dM_i}{dt} = a_i r_i M_{i-1} - r_{i+1} M_i \quad \text{for} \quad i = 0,1,2,3 \tag{5}$$

where a_0, r_0, and r_4 are zero. At $t = 0$, $M_0 = 1$ and $M_{i\neq 0} = 0$.

a_i, B_i, and E_i are summarized in Table 1 for $i = 1, 2, 3$. At any point in time the sum of the condensed phases is the solid fraction, $S(t)$:

$$S(t) = \sum_{j=0}^{3} M_j(t) \tag{6}$$

Applying the foregoing to the modeling of TGA experiments, $S(t)$ is the mass fraction observed in the TGA test. TGA data for samples exposed at four heating rates were considered to form an objective function, H:

$$H = \sum_{i=1}^{4} \sum_{j=1}^{N_i} \{1 - S_i(t_{ij})/F_i(t_{ij})\}^2 \tag{7}$$

$S_i(t_{ij})$ and $F_i(t_{ij})$ are the predicted and measured mass fractions for the j-th discrete time of i-th experiment. The discrete times from each experiment were successive times at which 3°C temperature increases occurred in the experimental record from the starting temperature to approximately 1100°C. a_i, B_i, and E_i for $i = 1, 2, 3$ reported in Table 1 in the "Mass Curve Fit" columns were found by numerical search methods to minimize H. B_i and E_i are also reported from the OFW optimization method discussed earlier.

Table 1 Pre-exponential factors, activation energies, and stoichiometry coefficients for three reactions.

Reaction	Mass Curve Fit			OFW	
i	a_i	B_i(1/s)	E_i (J/kmol)	B_i(1/s)	E_i (J/kmol)
1	0.6936	5.905E5	9.228E7	1.54E+05	8.72E+07
2	0.7944	1.334E6	1.284E8	4.47E+02	7.93E+07
3	0.6357	2.566	5.845E7	3.27E+01	8.22E+07

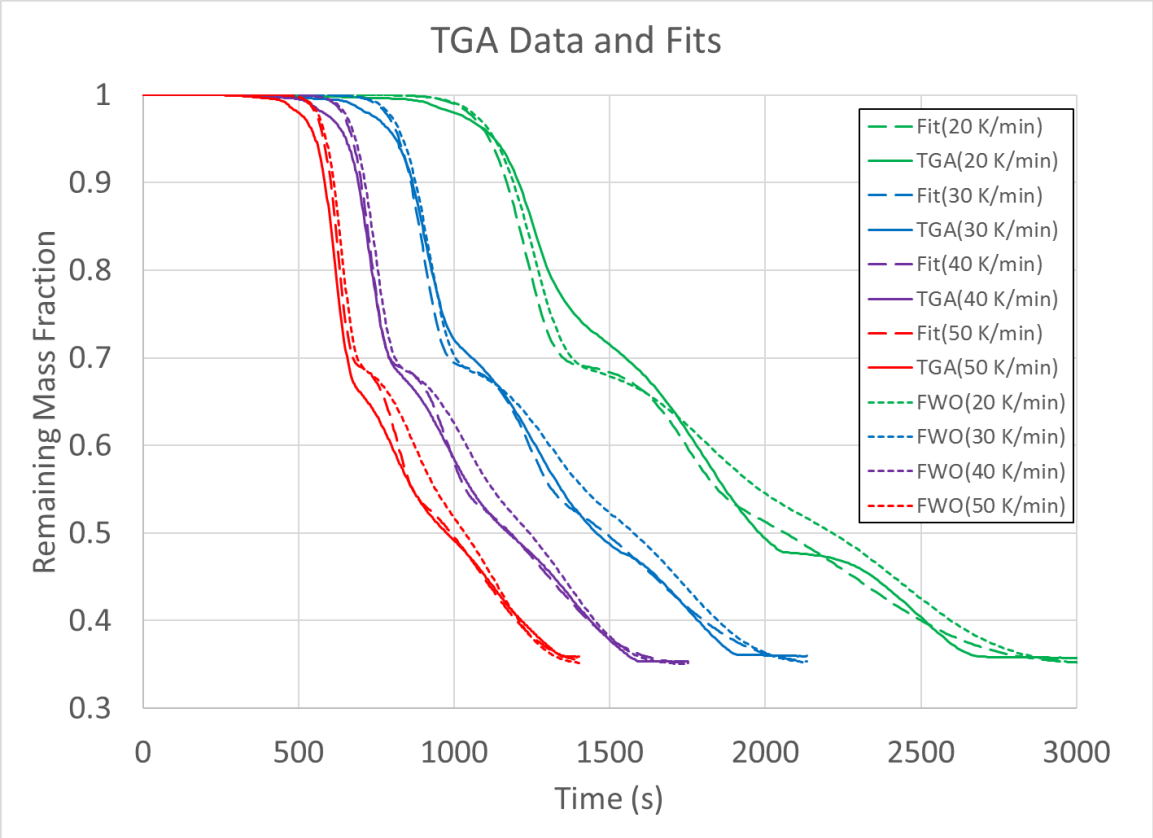

Figure 8. TGA measurements and model predictions.

Fig. 8 shows fair agreement of the foregoing formulation with the measured mass loss curves for four TGA experiments with heating rates of 20, 30, 40, and 50K/min. Fig. 8 includes predictions using the same system of equations with B_i and E_i from the FWO optimization.

4.3 Conduction and Radiation

Early in the heating process the intumescing material is a simple solid and heat transfer within it is by conduction only. During this time transport is described by Fourier's conduction law. However, when the heating is sufficient to decompose the material temperatures are elevated, the decomposition products are porous and expanding, and thermal radiation through the layer becomes important. One practical approach treats the radiation transport as a diffusion mechanism:

$$k_{\text{eff}}(\boldsymbol{x},T) = k_{\text{cond}}(\boldsymbol{x},T) + k_{\text{rad}}(\boldsymbol{x},T) = k_{\text{cond}}(\boldsymbol{x},T) + \frac{16}{3a(\boldsymbol{x},T)}\sigma\, T^3(\boldsymbol{x},t) \tag{8}$$

In this case $\dot{q}(\boldsymbol{x})$ of Eq. 2 is due only to chemical reactions and phase changes. This approach is commonly referred to as the diffusion approximation for treating thermal radiation. In Eq. 8 $a(\boldsymbol{x},T)$ is a linear absorption coefficient. During the decomposition of the IM, the temporally and spatially varying $a(\boldsymbol{x},T)$ results from the distribution of changing density and chemical composition and complicated gas and condensed phase interactions expanding the layer.

Griffin [1] used an equation similar to Eq. 8 in which $\frac{16}{3a(\boldsymbol{x},T)}$ is replaced by $\frac{16d}{3\omega\epsilon_c(\boldsymbol{x},T)}$ where d, ω, and ϵ_c are a cell size, porosity, and emissivity. In that investigation number density of cells was varied and used with the chemistry-implied porosity to the same effect as the $a(\boldsymbol{x},T)$ used here.

The FEM implementation of the model uses a fixed mesh to represent the expanding IM by defining a local variable, expansion ratio (ϕ). The effect of dilating the original material space is implemented by adjusting the local effective thermal conductivity:

$$k^*_{\text{eff}}(\boldsymbol{x},T) = k_{\text{eff}}(\boldsymbol{x},T)/\phi \tag{9}$$

The implementation of the model is three-dimensional though the results presented are for a simple geometry with a nearly one-dimensional response. The use of Eq. (9) is not proper when the IM is applied to surfaces with curvature or at intersections of plane surfaces. However, the systems for which the model is desired will implement broad, flat surfaces with dimensions on the order of 1000s of IM thicknesses. Consequently, the interference implied by expansion into interior corners is negligible for large systems.

The FEM code requires $k^*_{\text{eff}}(\boldsymbol{x},T)$, the chemistry of the decomposition, and the mesh with intial and boundary conditions to complete the problem definition. The progression from virgin material to the fully decomposed and expanded products is a complicated process with phase and chemical species changing; gas generation, flow, and attendant material erosion; and varying geometry of condensed material during the evolution. The current modeling strategy is to relate a and ϕ to the composition of the material empirically requiring the expansion to increase and the linear absorptivity to decrease with progression of the decomposition. The results to be presented assume:

$$\phi(t) = \phi_{\max} - M_0(t)(\phi_{\max} - 1) \tag{10}$$

So as M_0 disappears from the system the expansion ratio grows from 1 to $\phi_{\max}$ and

$$\frac{a(t)}{a_F} = \left(\frac{a_0}{a_F}\right)^{\frac{S(t)-S_F}{1-S_F}} \tag{11}$$

$\phi_{\max}$ is the maximum expansion ratio expected for the IM and S_F is the mass fraction when all of decomposition reactions have completed (0.35 for the current IM, See Fig. 8). Eqs. 10 and 11 impose paths for the evolving quantities they specify. Various functional forms were tried. a_0 must be sufficiently large that the radiation contribution to the effective thermal conductivity is negligible for the virgin material.

Late in the experiment of Fig. 6 the chemical decomposition is substantially complete and the IM layer is expanded to around 35% of its initial density so that it has relatively little thermal capacitance as compared to the adjacent steel layer. During this late time the response of TC16 or TC20 may be considered to be due to a

quasi-steady flow of heat through the expanded IM layer. The result of solving the steady diffusion equation [18] for thermal radiation for a planar layer of constant thickness, bound by gray surfaces (ε_1, ε_2 and T_1 , T_2) is:

$$q" = \frac{\sigma(T_1^4 - T_2^4)}{\frac{1}{\varepsilon_1}+\frac{1}{\varepsilon_2}+\frac{3}{4}aH-1} \tag{12}$$

where H is the layer thickness. Regarding TC16's response in the interval from 500 to 1500s as driven by a quasi-steady thermal process predicted by equation 2 implies $a_F \cong 1170$ m^{-1}. So $aH \sim 30$ and, provided the emissivities are not very small, the $\frac{1}{\varepsilon_1}+\frac{1}{\varepsilon_2}-1$ terms in the denominator of Eq. 12 are relatively unimportant compared to the optical thickness of the material.

5. MODELING RESULTS

The chemical decomposition model and the functional forms of and parameters in Eqs. 10 and 11 are the crux of the model. Parameter optimization was performed to find a constant k_{cond} (Eq. 8) and a_F (Eq.11) that produced the best agreement between the model and the responses of TC16 and TC20 as given in Fig. 6. In addition to the properties previously described, the model used measured C_p (1200-1600 J/kg·K) to about 180°C and held the value constant thereafter. The initial IM density was 1130 kg·m^{-3}. a_0 is arbitrarily large to eliminate a radiative contribution in Eq. 11 for the virgin material ($a_0 = 10^6 \text{m}^{-1}$). ϕ_{max}=22, as observed. A radiation boundary condition with a gray (ε=0.8) surface seeing the average temperature of the shroud (Fig. 5) drives the response. Table 2 summarizes parameters found by numerical search to optimize model agreement with the TC16 and TC20 responses.

Table 2 Model parameters found by optimization.

Parameter	TC16	TC20
k_{cond} (W·m^{-1}·K^{-1})	0.324	0.037
a_F(m^{-1})	916	854
R_1(J·kg^{-1})	-0.54E6	
R_2(J·kg^{-1})	50.5	
R_3(J·kg^{-1})	0	

In addition to the transport properties, Table 2 includes release energies used for each reaction, R_i. The R_i in Table 2 are the result of a separate optimization on R_1 and R_2 holding the other parameters constant and maximizing agreement with the first 400s of TC16's response. Griffin's [1] IM most like that investigated here was described as exhibiting an exothermic reaction (0.69 MJ/kg) which was nearly offset with an endothermic melting energy (0.65 MJ/kg). At the end time in Fig. 9 the energy to heat the metal substrate 800°C is approximately 100 times the energy associated with an IM energy "yield" of R_1. Consequently, the energy of reaction is not expected to change the result significantly for large temperature excursions of the substrate. Including these reaction energies may improve predictions early in the heating process. The reaction energies should be estimated with techniques such as DSC but further lab investigation of the subject IM was abandoned.

Fig 9 shows a comparison of model results with the data for the two locations. Also shown is the model prediction for a boundary temperature rising to 800°C in three minutes. Fig. 10 shows the M_0, M_1, M_2 and

M_3 are evolution for both boundary conditions demonstrating that the prediction indicates much less than the full decomposition process for the IM. The 800°C condition demonstrates a case in which the decomposition and associated conversion to reduced thermal resistance through the layer proceed more slowly.

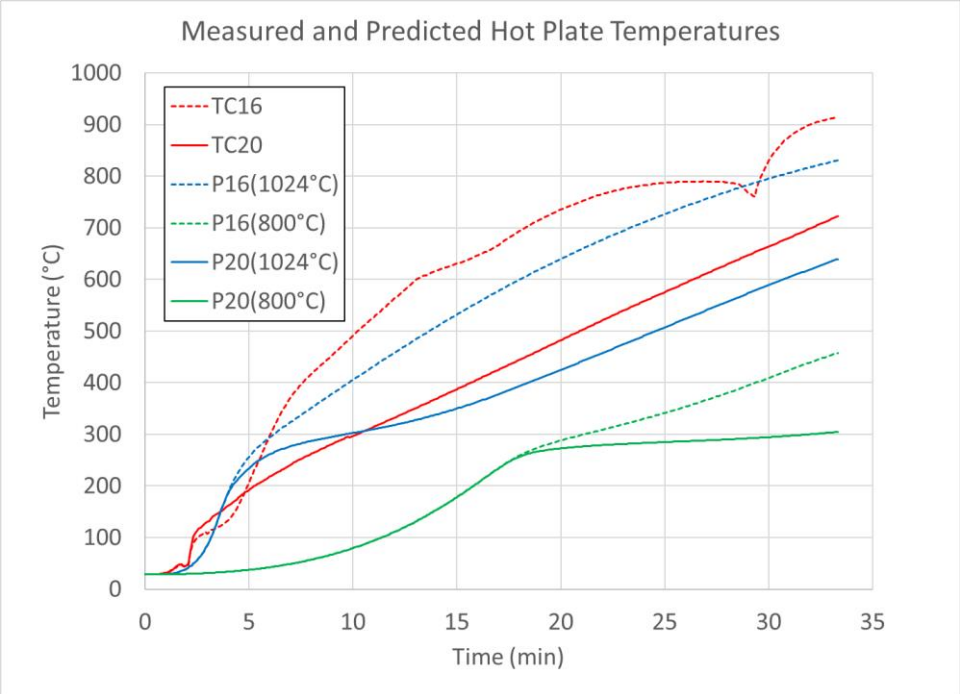

Fig. 9 Substrate temperature measurement for experimental conditions and predictions for 1024°C (measured) and 800°C shroud temperatures.

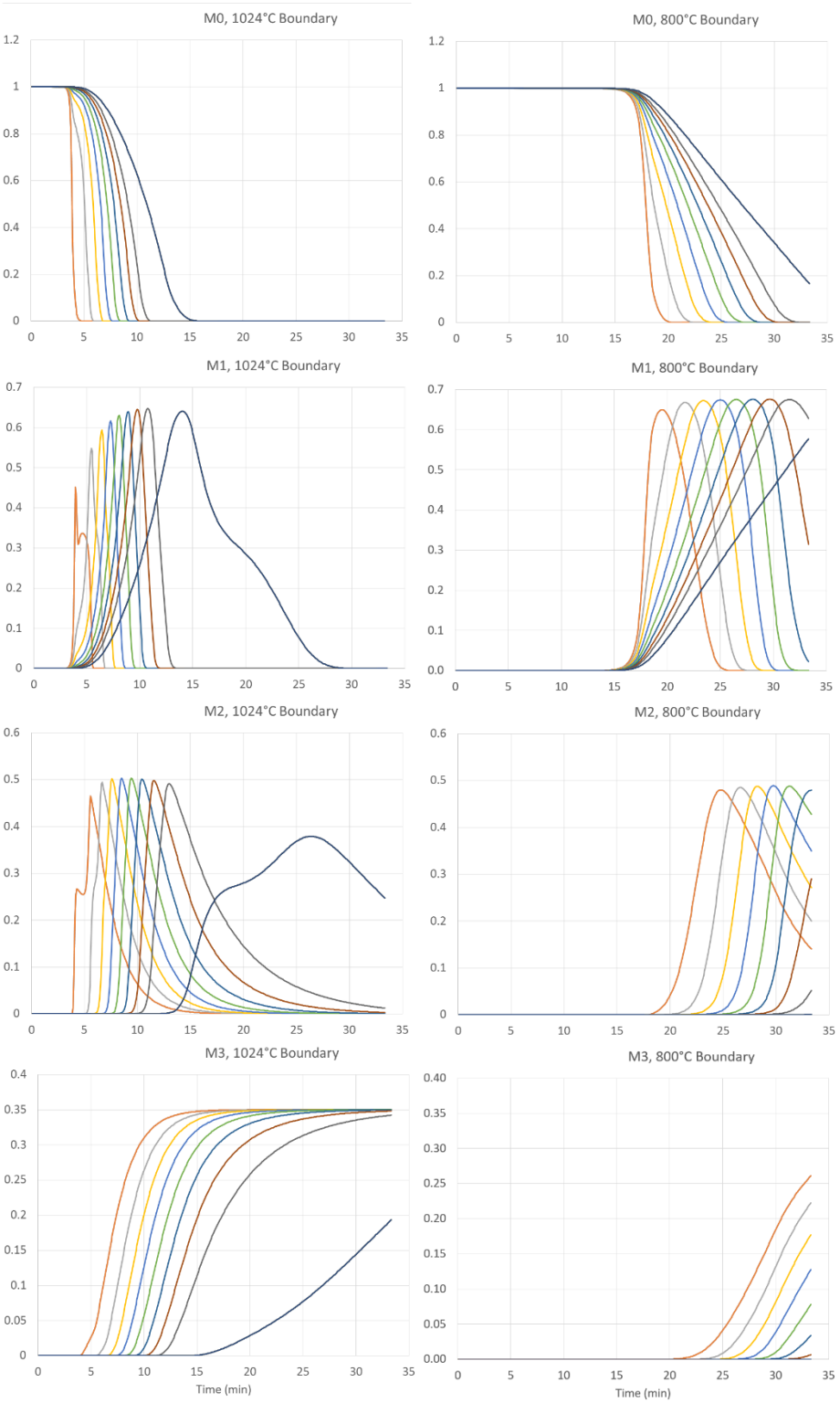

Fig. 10 "Species" profiles versus time for 1024°C and 800°C boundary temperatures. Curves from left to right are at 0, 0.1, 0.2…1.0 dimensionless initial material positions.

6. CONCLUSIONS

A finite element based model has been implemented to estimate thermal transport through a protective intumescent coating exposed to a fire environment. Parameters in the model characterize the chemical decomposition and thermal transport through the decomposing region. For the subject IM these critical parameters were not suitably established as the funding project changed to an alternate IM. Studies are proceeding to establish a similar model for that IM with the benefit of more extensive material characterization. The form of the model presented here is demonstrating preliminary success and those findings will be presented in future papers.

ACKNOWLEDGMENT

Supported by the Laboratory Directed Research and Development program at Sandia National Laboratories, a multi-program laboratory managed and operated by Sandia Corporation, a wholly owned subsidiary of Lockheed Martin Corporation, for the U.S. Department of Energy's National Nuclear Security Administration under contract DE-AC04-94AL85000. This document has been reviewed and approved for unclassified, unlimited release under 2016-3057.

REFERENCES

[1] Griffin, G.J., "The modeling of heat transfer across intumescent polymer coatings," *J. Fire Sci*., 28(3), pp. 249-277, (2010).
[2] Staggs, J.E.J., Crewe, R.J., Butler, R., "A theoretical and experimental investigation of intumescent behavior in protective coatings for structural steel," *Chem. Eng. Sci*., 71, pp. 239-251, (2012).
[3] Di Blasi, C., Branca, C., "Mathematical model for the nonsteady decomposition of intumescent coatings," *AIChE J*., 47(10), pp. 2359-2370, (2001).
[4] Di Blasi, C., "Modeling the effects of high radiative heat fluxes on intumescent material decomposition," *J. Anal. Appl. Pyrolysis*, 71, pp. 721-737, (2004).
[5] Jimenez, M., Duquesne, S., Bourbigot, S., "Multiscale experimental approach for developing high-performance intumescent coatings," *Ind. Eng. Chem. Res*., 45, pp. 4500-4508, (2006).
[6] Asaro, R.J., Lattimer, B., Mealy, C., Steele, G., "Thermo-physical performance of a fire protective coating for naval ship structures," *Composites, Part A*, 40, pp. 11-18, (2009).
[7] Branca, C., Di Blasi, C., "Analysis of the combustion kinetics and thermal behavior of an intumescent system," *Ind. Eng. Chem. Res*., 41, pp. 2107-2114, (2002).
[8] Mouritz, A.P., Feih, S., Kandare, E., Gibson, A.G., "Thermal-mechanical modelling of laminates with fire protection coating," *Composites, Part B*, 48, pp. 68-78, (2013).
[9] Landucci, G., Molag, M., Reinders, J., Cozzani, V., "Experimental and analytical investigation of thermal coating effectiveness for 3 m3 LPG tanks engulfed by fire," *J. Hazard. Mater*., 161, pp. 1182-1192, (2009).
[10] Kandola, B.K., Luangtriratana, P., Duquesne, S., Bourbigot, S., "The effects of thermophysical properties and environmental conditions on fire performance of intumescent coatings on glass fibre-reinforced epoxy composites," Materials, 8, pp. 5216-5237, (2015).
[11] Bhargava, A., Griffin, G.J., "A model of heat transfer across an epoxy based fire retardant layer undergoing sublimation, intumescence, and degradation," Dev. Chem. Eng. Mineral Process., 8, pp. 75-91, (2000).
[12] Younger, S.Y., Meyer, D., Finch, D., "Industrial fireproofing: Setting the story straight," *Mater. Perform*., pp. 4-18, (2012).
[13] Di Blasi, C., "The state of the art of transport models for charring solid degradation," *Polym. Int*., 49, pp. 1133-1146, (2000).
[14] Ozawa, T., "A new method of analyzing thermogravimetric data," Bull. Chem. Soc. Jpn., 88, pp. 1881-1886, (1965).
[15] Flynn, J.H., Wall, L.A., "A quick, direct method for the determination of activation energy from thermogravimetric data," Polym. Lett., 4, pp. 323-328, (1966).
[16] ASTM E1641. "Standard test method for decomposition kinetics by thermogravimetry using the Ozawa/Flynn/Wall Method."
[17] Chairat, A., Joulia, X., Floquet, P., Vergnes, H., Ablitzer, C., Fiquet, O., Brothier, M., "Thermal degradation kinetics of a commercial epoxy resin – Comparative analysis of parameter estimation methods," *J. Appl. Polym. Sci*., 132(27), pp. 216-302, (2015).
[18] Siegel, R. and J. R. Howell, *Thermal Radiation Heat Transfer*, 4th Edition, McGraw Hill, pp. 639 (2002).